University of Wollongong
Research Online

Faculty of Engineering - Papers (Archive)

Faculty of Engineering and Information Sciences

2003

Performance evaluation of a multipinhole small animal SPECT system

S. R. Meikle
Royal Prince Alfred Hospital, Sydney

P. Kench
University of Sydney

R. Wojcik
Thomas Jefferson National Accelerator Facility, Virginia, USA

M. F. Smith
Thomas Jefferson National Accelerator Facility, Virginia, USA

A. G. Weisenberger
Thomas Jefferson National Accelerator Facility, Virginia, USA

See next page for additional authors

http://ro.uow.edu.au/engpapers/71

Publication Details

This paper originally appeared as: Meikle, SR, Kench, P, Wojcik, R et al, Performance evaluation of a multipinhole small animal SPECT system, IEEE Nuclear Science Symposium Conference Record, 19-25 October 2003, vol 3, 1988-1992. Copyright IEEE 2003.

Research Online is the open access institutional repository for the University of Wollongong. For further information contact the UOW Library: research-pubs@uow.edu.au

Authors
S. R. Meikle, P. Kench, R. Wojcik, M. F. Smith, A. G. Weisenberger, S. Majewski, M. L. Lerch, and Anatoly B. Rosenfeld

This conference paper is available at Research Online: http://ro.uow.edu.au/engpapers/71

Performance Evaluation of a Multipinhole Small Animal SPECT System

Steven R. Meikle, *Senior Member, IEEE*, Peter Kench, Randy Wojcik, Mark F. Smith, *Member, IEEE*, Andrew G. Weisenberger, Stan Majewski, Michael Lerch, *Member, IEEE* and Anatoly B. Rosenfeld, *Senior Member, IEEE*

Abstract—**We have designed and constructed a small animal SPECT system based on compact, high resolution detectors and multipinhole apertures. The scanner is currently configured with two detectors mounted on a rotating gantry. Each detector comprises a NaI(Tl) crystal array (1x1x5 mm elements), a 12 cm diameter position-sensitive photomultiplier tube (Hamamatsu R3292) and a tungsten aperture with 1 or more pinholes. In this study, we performed phantom experiments to characterise the planar and tomographic performance of the scanner. Intrinsic resolution measured with a highly collimated ^{99m}Tc point source stepped across the detector face was 1.0±0.1 mm FWHM and 2.9±0.1 mm FWTM. Energy resolution at 140 keV varied from 14% FWHM for central crystals to 19% for edge crystals and was 20% FWHM for the whole detector normalised spectrum. Intrinsic uniformity for the central field of view was 2.4% differential and 3.8% integral. Reconstructed spatial resolution was 1.2 mm FWHM at the centre of the field of view and 1.2, 1.7 mm FWHM (radial, tangential) at 10 mm off-axis, using typical geometric parameters for mouse and rat brain imaging. Reconstructed images of a micro deluxe hot rod phantom demonstrate the high resolution of the system and indicate similar resolution and improved signal-to-noise is obtained with a 2 pinhole aperture compared with a single pinhole. We conclude that the performance characteristics of this system make it suitable for high resolution imaging of small laboratory animals.**

I. Introduction

Molecular imaging of animal models of human disease is a rapidly evolving field and dedicated instruments have been developed for several imaging modalities [1, 2]. Radionuclide techniques, such as single photon emission computed tomography (SPECT) and positron emission tomography (PET), are among the most sensitive of these modalities, having the capability to detect tracer concentrations (<10^{-9} mol) of a radiolabelled probe in vivo. Furthermore, the same probes and imaging techniques can be applied across a wide range of species from mice to humans, making these truly translational research tools.

SPECT has several advantages compared with other imaging modalities. For example, high resolution images (<1 mm) can be achieved when pinhole geometry is employed [3-6], the half-life of single photon emitters is amenable to studying biological processes that occur over hours or days rather than minutes, and it is theoretically possible to image 2 probes simultaneously using dual energy acquisition. However, SPECT is limited by the inherently low detection efficiency (typically 2 orders of magnitude lower than PET) due to the requirement for mechanical collimation of photons emitted from the animal. In practice, this limits the detection of small signals despite the high sensitivity and resolution of SPECT and limits its potential for studying and quantifying dynamic biological processes.

We are developing a dedicated small animal SPECT system based on compact high resolution detectors [7, 8]. Collimation with multipinhole apertures is also being investigated by our group and by Schramm et al to devise optimal approaches for improving the detection efficiency of small animal SPECT [9, 10]. Such approaches will be beneficial in other applications where detection efficiency is a limiting factor, including a related project to image unanaesthetised mice using a motion tracking apparatus and list-mode acquisition [11, 12].

In this study, we performed phantom experiments to characterise the planar and tomographic performance of the scanner. We also discuss the performance of the prototype

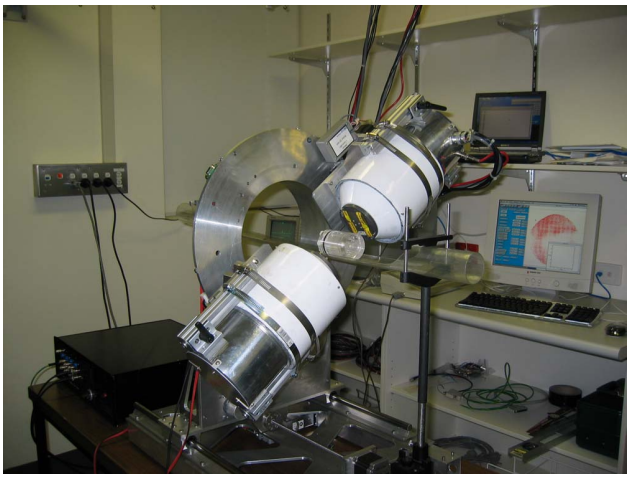

Fig. 1. Small animal SPECT scanner.

Manuscript received October 29, 2003. This work was supported by the University of Sydney under a major equipment grant and by the Office of Biological and Environmental Research of the U.S. Department of Energy. The Southeastern Universities Research Association operates the Thomas Jefferson National Accelerator Facility for the U.S. Department of Energy under contract DE-AC05-84ER40150.

S. R. Meikle is with the Department of PET and Nuclear Medicine, Royal Prince Alfred Hospital, Sydney, NSW 2050 Australia (telephone: 02-9515-6173, e-mail: steve@cs.usyd.edu.au).

P. Kench is with the School of Medical Radiation Sciences, University of Sydney, Sydney, NSW Australia (p.kench@fhs.usyd.edu.au).

R. Wojcik (wojcik@jlab.org), M. F. Smith (mfsmith@jlab.org), A. G. Weisenberger (drew@jlab.org) and S. Majewski (majewski@jlab.org) are with the Thomas Jefferson National Accelerator Facility, Newport News, VA 23606 USA. R. Wojcik is also with Ray Visions Inc., Yorktown, VA 23693 USA.

M. Lerch (mlerch@uow.edu.au) and A. B. Rosenfeld (anatoly@uow.edu.au) are with the Centre for Medical Radiation Physics, University of Wollongong, Wollongong, NSW Australia.

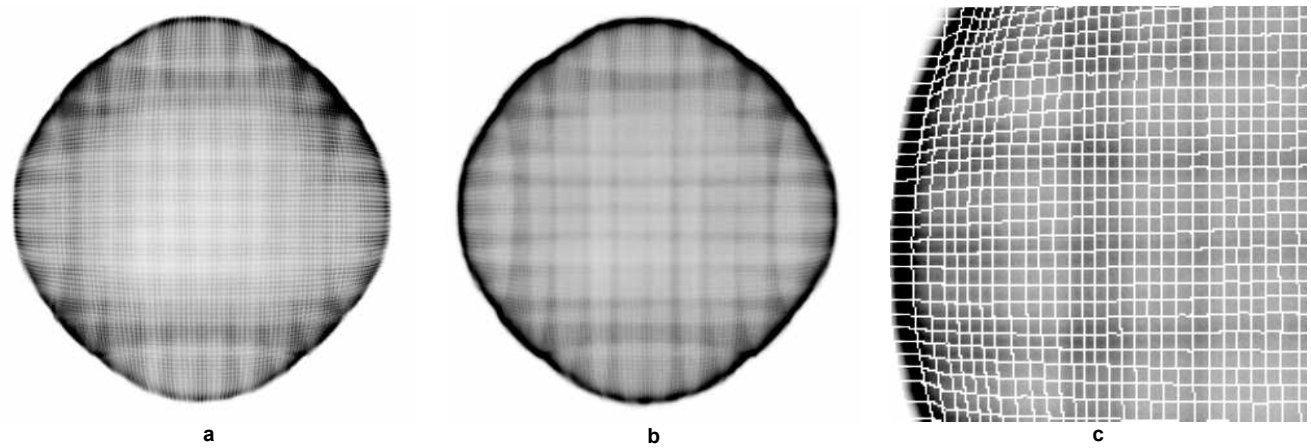

Fig. 2. Position histograms obtained for a 511 keV source (a) and a 140 keV source (b). A zoomed section of the 140 keV image with crystal lookup table overlayed is also shown (c).

scanner in relation to target resolution-efficiency trade-offs.

II. Scanner Design

The scanner was designed as a three head system with detectors spaced 120 degrees apart. The prototype is currently configured as a dual head scanner with opposing detectors (Fig. 1). The detectors rotate around the animal in the vertical plane under computer control. The radial distance between detectors can be varied as can the distance from the pinhole apertures to the detector faces. This allows the field of view and magnification to be adjusted which in turn determine the resolution and detection efficiency of the system. The minimum field of view (in image space) is 3.5 cm and the maximum magnification is 3.2.

Each detector comprises a NaI(Tl) crystal array and light guide, a position-sensitive photomultiplier tube (PS-PMT) (Hamamatsu R3292) and a subtractive resistive read-out circuit [13]. The crystal array is a 12 cm diameter disk of 5 mm thick NaI(Tl) cut into 1x1x5 mm elements with a 1.25 mm centre to centre spacing. The gaps between crystals are filled with Teflon powder to prevent light spreading to adjacent crystals. The detector is enclosed in 6.5 mm Pb shielding and the tungsten aperture is mounted in a telescopic nose cone. The signals from both detectors are multiplexed and sampled by two National Instruments PCI-6110E 4 channel ADC boards running on a Macintosh dual processor G4 computer under Kmax software control (Sparrow Corporation, Daytona Beach, FL).

III. Calibration Procedures

A high count image is recorded with a 20 MBq ^{18}F source placed approximately 1 metre away from the uncollimated detector. This image, which shows a clear separation between crystals (Fig. 2a), is used to derive a crystal lookup table for positioning of events. Fig. 2b shows a high count image acquired with a 140 keV source and Fig. 2c shows a zoomed section of the same image with the crystal lookup table (derived from the 511 keV image) overlayed. These images demonstrate that, although the crystals are less clearly delineated at 140 keV, the positioning of events is unaffected by the energy of the isotope or the high voltage applied to the PS-PMT. This allows us to use the same crystal lookup table for data acquired at all energies, at least within the range 140-511 keV. After defining the crystal lookup table, energy spectra are acquired for each crystal and the photopeak channel is recorded. Subsequent acquisitions are normalised for energy by shifting the energy axis of events recorded in each crystal location to achieve alignment of the photopeaks. Finally, a high count flood is acquired with a point source placed approximately 2 metres from the uncollimated detector and subsequently used to correct projection data for detector non-uniformity.

For SPECT studies we use the method described by Bequé et al to measure 7 parameters that describe the pinhole SPECT geometry [14]. These include the focal length of the pinhole(s), the perpendicular distance from pinhole(s) to the axis of rotation, electrical and mechanical offsets of the detectors relative to the centre of the field of view and angular tilt and rotation of the detectors. The procedure involves imaging a phantom comprising 3 point sources at several angles and iteratively improving the estimated geometric parameters by minimising the sum of the squared distances between measured and projected point source positions. We use the downhill simplex algorithm to optimise the solution and it typically takes 200 iterations to achieve convergence.

IV. Experimental Methods

A. Planar Performance

A ^{99m}Tc source was placed behind a double slit collimator that produced a highly collimated beam of approximately 0.5 mm diameter at the detector face. The source was stepped across the detector face and measurements made at 0.2 mm intervals. The counts in each detector element (corresponding to a physical crystal) were plotted as a function of source position. For each of the profiles, the full width at half maximum (FWHM) and full width at tenth maximum (FWTM) values were calculated and averaged.

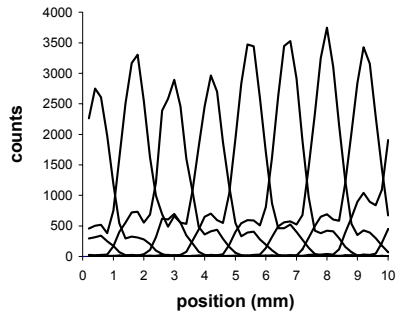

Fig. 3. Count profiles from the collimated point source stepped across the centre of the detector.

Energy resolution was measured for a 140 keV point source by recording individual energy spectra for each of the detector elements. A Gaussian function was fitted to the photopeaks of energy spectra recorded at the centre and periphery (2 cm from the edge of the field of view) of the detector. We also calculated the resolution of the normalised whole detector energy spectrum which is obtained by aligning the photopeaks of all the individual spectra and summing them.

Intrinsic uniformity was measured with a ^{99m}Tc point source placed 1.5 m from the uncollimated detector face. The resulting flood image was analysed after corrections were applied for non-uniform energy and linearity response of the detector. Integral and differential uniformity were calculated according to the NEMA NU-1 2001 protocol.

B. Tomographic Performance

Two ^{99m}Tc point sources (diameter 0.5 mm) were placed in the field of view, one at the centre of the field of view and one displaced 10 mm from the axis of rotation. The distance from the aperture to the axis of rotation was 4 cm and the distance from the crystal face to the aperture was 8 cm, resulting in a magnification of 2 and a field of view of 5.5 cm. These are the geometric parameters we expect to use for imaging the mouse and rat brain. Data were acquired for 40 seconds per projection at 9˚ increments over 360˚ and reconstructed using 5 iterations and 5 subsets of 3D OS-EM. The 3D multipinhole OS-EM algorithm is described in previous reports [7, 8]. A Gaussian function was fitted to radial and tangential count profiles of each of the reconstructed point sources.

SPECT studies were performed using the micro deluxe hot rod phantom (Data Spectrum Corp., NC). This phantom has an internal diameter of 4.5 cm and 6 pie sectors of rods with diameters ranging from 1.2 mm to 4.8 mm. For the first study, a single pinhole aperture (0.5 mm diameter, 45˚ acceptance angle) was used and the distance between the aperture and axis of rotation was 6 cm. The distance from the crystal face to the aperture plane was 8 cm. The phantom contained 400 MBq ^{99m}Tc at the beginning of the study. Data were acquired for 60 seconds per projection at 9˚ increments over 360˚. Images were reconstructed using 5 iterations and 8 subsets of OS-EM into a 64^3 matrix with 1 mm voxels and smoothed using a 3D Gaussian kernel with 1 mm FWHM.

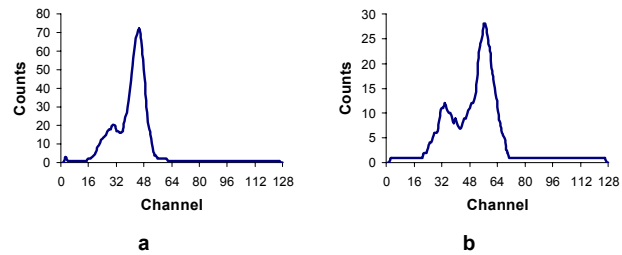

Fig. 4. Typical energy spectra for individual crystals located at the centre (a) and periphery (b) of the field of view.

A further study was performed with the hot rod phantom using an aperture with 2x0.5 mm diameter pinholes located 12 mm apart, equidistant from the rotation (z) axis and separated by 5 mm along the z axis. Data were acquired at 9˚ increments over 360˚ for 60 seconds per projection. Images were reconstructed using 5 iterations and 8 subsets of OS-EM into a 64^3 matrix with 1 mm voxels and smoothed using a 3D Gaussian kernel with 1 mm FWHM. We also performed a reconstruction using the same parameters after combining the single pinhole data on one head with the double pinhole data on the other head.

C. Detection efficiency

Detection efficiency was measured for the 1 pinhole and 4 pinhole configuration using the same geometric parameters as for the spatial resolution experiment. A point source containing 20 MBq ^{99m}Tc was placed in the centre of the field of view and data acquired on both detector heads at a single fixed position. Detection efficiency was calculated as the counts recorded in an energy window of 119-161 keV (30%) divided by the decay-corrected activity of the source.

V. Results and Discussion

A. Planar Performance

Count profiles for individual crystals are shown in Fig. 3. The observed detector response includes a main peak and two smaller side lobes corresponding to the adjacent crystals. We attribute these side lobes to a combination of factors: (i) the relatively low light output at 140 keV causes spreading of the detector response across adjacent crystals, (ii) forward scattering of low energy photons from neighbouring crystals, and (iii) reduced sensitivity at the gaps between crystals enhances the valley between the main peak and the smaller side lobes. The FWHM resolution of these profiles was 1.0±0.1 mm and the full width at tenth maximum (FWTM) (measured across the side lobes) was 2.9±0.1 mm.

Typical energy spectra for central and peripheral crystals are shown in Fig. 4. Energy resolution at 140 keV varied from 14% FWHM for central crystals to 19% for edge crystals. The resolution of the normalised whole detector energy spectrum was 20% FWHM. Intrinsic uniformity for the central field of view (75% of useful field of view) was 2.4% differential and 3.8% integral.

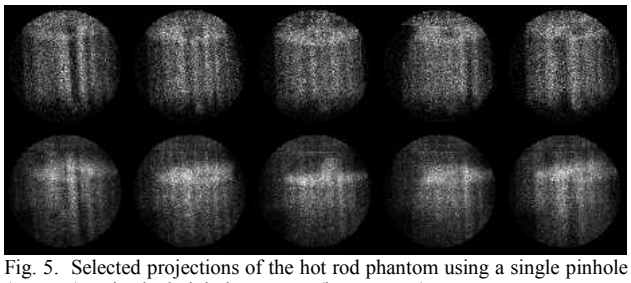

Fig. 5. Selected projections of the hot rod phantom using a single pinhole (top row) and a dual pinhole aperture (bottom row).

B. Tomographic Performance

Reconstructed spatial resolution for the single pinhole study was 1.2 mm FWHM at the centre of the field of view and 1.2, 1.7 mm FWHM (radial, tangential), at 10 mm off-axis. For the 4 pinhole study, reconstructed spatial resolution was 1.5 mm FWHM at the centre of the field of view and 1.8, 1.6 mm FWHM (radial, tangential), at 10 mm off-axis.

Selected projections of the hot rod phantom are shown in Fig. 5 for the single and double pinhole acquisitions. The degree of overlap of projection data was approximately 30% in the dual pinhole case. Five consecutive transaxial slices of the hot rod phantom reconstructions are shown in Fig 6. These results indicate that there is no appreciable loss of spatial resolution comparing the dual pinhole with single pinhole reconstructions. There are, however, some slight distortions present in the dual pinhole images which are resolved in the images obtained by combining single and dual pinhole data. In the third row of Fig. 6, there appears to be better definition of the 2.4 mm diameter rods in the 4th pie sector, most likely due to an increase in local signal-to-noise ratio. The spatial resolution of these images is estimated to be 2 mm, slightly worse than that measured from the point source reconstructions due to the increased distance from the aperture to the axis of rotation required by the size of the phantom.

C. Detection efficiency

The detection efficiency measured for the single pinhole aperture was 39 counts.sec^{-1}.MBq^{-1} (0.004%) while for the 4 pinhole aperture it was 146 counts.sec^{-1}.MBq^{-1} (0.015%). To compare these measurements with the predicted theoretical values, we calculated efficiency-resolution trade-off curves using the following formulae [15]:

$$R = \frac{\sqrt{\left(d_e\left(L+H+B\right)/H\right)^2 + R_i^2}}{M} \quad (1)$$

$$G = \frac{d_e^2}{16H^2} N\varepsilon \quad (2)$$

where d_e is the effective hole diameter, L is the focal length of the pinhole, H is the pinhole to source distance, B is the average depth of interaction in the crystal (assumed 2.5 mm for 140 keV photons in NaI(Tl)), R_i is the intrinsic resolution of the detector, M is the magnification factor, N is the number of detectors and ε is the detection efficiency for 5 mm thick crystals (0.7 at 140 keV).

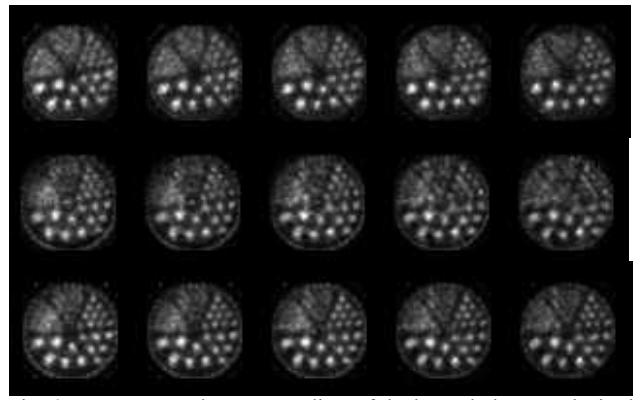

Fig. 6. Reconstructed transverse slices of the hot rod phantom obtained using a single pinhole (top row), a 2 pinhole aperture (middle row) and the combined data from the single and dual pinhole apertures (bottom row).

In the curves shown in Fig. 7, the resolution-efficiency trade-off was achieved by varying the pinhole diameter from 0.2-2 mm while fixing the geometric parameters at L=8 cm, H=4 cm and M=2, which are the parameters we will use for imaging the mouse and rat brain. The measured efficiency and resolution values are in good agreement with the predicted trade-off curves for this geometry. It should be noted that we used a relatively narrow energy window of 30% (symmetric ±15%) for these measurements which, due to the relatively poor energy resolution of our detectors, may result in the loss of potentially good events.

These curves indicate that to achieve a target detection efficiency of approximately 0.1% while maintaining spatial resolution ≤2 mm will require a triple head scanner with 6 pinholes per head each with a 1.5 mm diameter pinhole. This would put the detection efficiency of the system about an order of magnitude lower than PET. We believe this is a reasonable target since the specific activity of ^{123}I-labelled compounds is typically an order of magnitude greater than that of ^{11}C-labelled compounds.

VI. Conclusions

The planar and tomographic performance of the dual detector prototype scanner meet our design goals and we anticipate that reconstructed SPECT spatial resolution of better than 1.5 mm FWHM will be achievable under typical imaging conditions. We conclude that the performance characteristics of the system in its current dual head configuration make it suitable for certain small animal imaging applications. Pilot studies with a rat model of Parkinson's disease and a ^{123}I-labelled dopamine transporter ligand will be performed in the near future.

The detection efficiency of the scanner can be further improved by adding a 3rd detector and using multipinhole arrays. However, further work is required to optimise multipinhole aperture designs and fully characterise the resolution-variance trade-offs associated with reconstruction of multiplexed projection data.

VII. REFERENCES

[1] R. Weissleder and U. Mahmood, "Molecular imaging," *Radiology*, vol. 219, pp. 316-333, 2001.

[2] S. R. Cherry, "In vivo molecular and genomic imaging: New challenges for imaging physics," *Phys Med Biol*, vol. 48, (in press), 2003.

[3] R. J. Jaszczak, K. L. Greer, C. E. Floyd, C. G. Harris, and R. E. Coleman, "Improved SPECT quantitation using compensation for scattered photons," *J Nucl Med*, vol. 25, pp. 893-900, 1984.

[4] D. A. Weber, M. Ivanovic, D. Franceschi, S.-E. Strand, K. Erlandsson, M. Franceschi, H. L. Atkins, J. A. Coderre, H. Susskind, T. Button, and K. Ljunggren, "Pinhole SPECT: an approach to in vivo high resolution SPECT imaging in small laboratory animals," *J Nucl Med*, vol. 35, pp. 342-348, 1994.

[5] K. Ishizu, T. Mukai, Y. Yonekura, M. Pagani, T. Fujita, Y. Magata, S. Nishizawa, N. Tamaki, H. Shibasaki, and J. Konishi, "Ultra-high resolution SPECT system using four pinhole collimators for small animal studies," *J Nucl Med*, vol. 36, pp. 2282-2287, 1995.

[6] D. P. McElroy, L. R. MacDonald, F. J. Beekman, Y. Wang, B. E. Patt, J. S. Iwanczyk, B. M. W. Tsui, and E. J. Hoffman, "Performance evaluation of A-SPECT: a high resolution desktop pinhole SPECT system for imaging small animals," *IEEE Trans Nucl Sci*, vol. 49, pp. 2139-2147, 2002.

[7] S. R. Meikle, P. Kench, A. G. Weisenberger, R. Wojcik, M. F. Smith, S. Majewski, S. Eberl, R. R. Fulton, A. B. Rosenfeld, and M. J. Fulham, "A prototype coded aperture detector for small animal SPECT," *IEEE Trans Nucl Sci*, vol. 49, pp. 2167-2171, 2002.

[8] S. R. Meikle, R. Wojcik, A. G. Weisenberger, M. F. Smith, S. Majewski, P. Kench, S. Eberl, R. R. Fulton, M. Lerch, and A. B. Rosenfeld, "CoALA-SPECT: A coded aperture laboratory animal SPECT system for pre clinical imaging," Conference Record of the 2002 IEEE Nuclear Science Symposium and Medical Imaging Conference, Norfolk, 2002.

[9] M. F. Smith, S. R. Meikle, S. Majewski, and A. G. Weisenberger, "Design of multipinhole collimators for small animal SPECT," Conference Record of the 2003 IEEE Nuclear Science Symposium and Medical Imaging Conference, Portland, OR, 2003.

[10] N. U. Schramm, G. Ebel, U. Engeland, T. Schurrat, M. Behe, and T. M. Behr, "High-resolution SPECT using multipinhole collimation," *IEEE Trans Nucl Sci*, vol. 50, pp. 315-320, 2003.

[11] A. G. Weisenberger, B. F. Kross, S. Majewski, V. Popov, M. F. Smith, B. L. Welch, R. Wojcik, S. S. Gleason, J. S. Goddard, M. J. Paulus, and S. R. Meikle, "Development and testing of a restraint free small animal SPECT imaging system with infrared based motion tracking," Conference Record of the 2003 IEEE Nuclear Science Symposium and Medical Imaging Conference, Portland, OR, 2003.

[12] J. S. Goddard, S. S. Gleason, M. J. Paulus, R. Kerekes, S. Majewski, V. Popov, M. F. Smith, A. G. Weisenberger, B. L. Welch, and R. Wojcik, "Pose measurement and tracking system for motion-correction of unrestrained small animal PET/SPECT imaging," Conference Record of the 2003 IEEE Nuclear Science Symposium and Medical Imaging Conference, Portland, OR, 2003.

[13] R. Wojcik, S. Majewski, B. Kross, V. Popov, and A. G. Weisenberger, "Optimized readout of small gamma cameras for high resolution single gamma and positron emission imaging," Conference Record of the 2001 IEEE Nuclear Science Symposium and Medical Imaging Conference, San Diego, 2001.

[14] D. Bequé, J. Nuyts, G. Bormans, P. Suetens, and P. Dupont, "Characterization of pinhole SPECT acquisition geometry," *IEEE Trans Med Imag*, vol. 22, pp. 599-612, 2003.

[15] L. E. Williams, *Nuclear Medical Physics*, vol. 2. Boca Raton, FL: CRC Press, 1987.

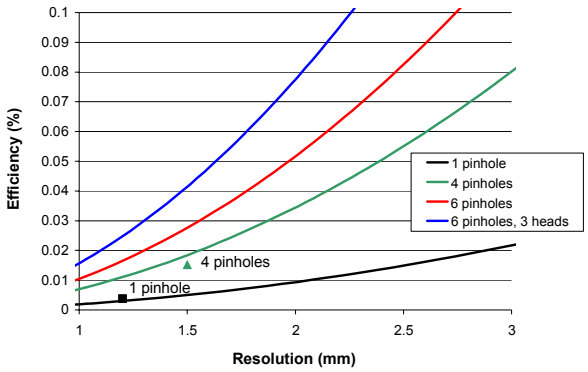

Fig. 7. Predicted detector efficiency vs resolution tradeoff curves for the current prototype (1, 4 and 6 pinhole apertures) and for a triple head design with 6 pinholes. The symbols indicate the measured detector efficiency and spatial resolution obtained with the current dual head configuration.